2013

Strain induced variations in band offsets and built-in electric fields in InGaN/GaN multiple quantum wells

L. Dong
University of Connecticut - Storrs

J. V. Mantese
United Technology Research Center

Vitaliy Avrutin
Virginia Commonwealth University, vavrutin@vcu.edu

See next page for additional authors

Dong, L., Mantese, J. V., & Avrutin, V., et al. Strain induced variations in band offsets and built-in electric fields in InGaN/GaN multiple quantum wells. Journal of Applied Physics, 114, 043715 (2013). Copyright © 2013 AIP Publishing LLC.

Strain induced variations in band offsets and built-in electric fields in InGaN/GaN multiple quantum wells

L. Dong,[1] J. V. Mantese,[2] V. Avrutin,[3] Ü. Özgür,[3] H. Morkoç,[3] and S. P. Alpay[1,4,a)]
[1]*Department of Physics, University of Connecticut, Storrs, Connecticut 06269, USA*
[2]*United Technology Research Center, East Hartford, Connecticut 06108, USA*
[3]*Department of Electrical and Computer Engineering, Virginia Commonwealth University, Richmond, Virginia 23284-3072, USA*
[4]*Department of Materials Science and Engineering and Institute of Materials Science, University of Connecticut, Storrs, Connecticut 06269, USA*

(Received 10 June 2013; accepted 4 July 2013; published online 26 July 2013)

The band structure, quantum confinement of charge carriers, and their localization affect the optoelectronic properties of compound semiconductor heterostructures and multiple quantum wells (MQWs). We present here the results of a systematic first-principles based density functional theory (DFT) investigation of the dependence of the valence band offsets and band bending in polar and non-polar strain-free and in-plane strained heteroepitaxial $In_xGa_{1-x}N$(InGaN)/GaN multilayers on the In composition and misfit strain. The results indicate that for non-polar *m*-plane configurations with $[1\bar{2}10]_{InGaN}//[1\bar{2}10]_{GaN}$ and $[0001]_{InGaN}//[0001]_{GaN}$ epitaxial alignments, the valence band offset changes linearly from 0 to 0.57 eV as the In composition is varied from 0 (GaN) to 1 (InN). These offsets are relatively insensitive to the misfit strain between InGaN and GaN. On the other hand, for polar *c*-plane strain-free heterostructures with $[10\bar{1}0]_{InGaN}//[10\bar{1}0]_{GaN}$ and $[1\bar{2}10]_{InGaN}//[1\bar{2}10]_{GaN}$ epitaxial alignments, the valence band offset increases nonlinearly from 0 eV (GaN) to 0.90 eV (InN). This is significantly reduced beyond $x \geq 0.5$ by the effect of the equi-biaxial misfit strain. Thus, our results affirm that a combination of mechanical boundary conditions, epitaxial orientation, and variation in In concentration can be used as design parameters to rapidly tailor the band offsets in InGaN/GaN MQWs. Typically, calculations of the built-in electric field in complex semiconductor structures often must rely upon sequential optimization via repeated *ab initio* simulations. Here, we develop a formalism that augments such first-principles computations by including an electrostatic analysis (ESA) using Maxwell and Poisson's relations, thereby converting laborious DFT calculations into finite difference equations that can be rapidly solved. We use these tools to determine the bound sheet charges and built-in electric fields in polar epitaxial InGaN/GaN MQWs on *c*-plane GaN substrates for In compositions $x = 0.125, 0.25, \ldots,$ and 0.875. The results of the continuum level ESA are in excellent agreement with those from the atomistic level DFT computations, and are, therefore, extendable to such InGaN/GaN MQWs with an arbitrary In composition. © *2013 AIP Publishing LLC*. [http://dx.doi.org/10.1063/1.4816254]

I. INTRODUCTION

The light-emitting-diode (LED) lighting industry has undergone a significant growth in the past decade primarily due to the development of devices using $In_xGa_{1-x}N$ (InGaN)/GaN/AlGaN heterostructures, relying upon detailed band structure analysis to continually improve luminosity and efficiency, while reducing fabrication costs.[1,2] InGaN alloys are miscible in the solid state[3] and have the prototypical wurtzite ($P6_3mc$) structure for their end components InN and GaN. Due to the non-centrosymmetric arrangement of In, Ga, and N atoms in this crystal structure, an InGaN crystal has a spontaneous polarization and is piezoelectric. The band gap (E_g) of the InGaN alloy varies from 0.7 eV (InN) to 3.4 eV (GaN) and covers the entire visible light spectrum and beyond. Depending on the In composition, violet, blue, green, yellow, and red light emissions can be realized in InGaN-based thin films and one-dimensional nanowire heterostructures.[1,2,4] To improve the optoelectronic efficiency of such constructs, active multilayers are fabricated as InGaN/GaN multiple quantum wells (MQW) on suitable substrates. The discontinuities in the conduction and valence band edges in such configurations result in quantum confinement and localization of electrons and holes at hetero-interfaces. These phenomena play a critical role in determining device performance because optoelectronic properties of InGaN MQWs are directly related to the degree of band offsets at the InGaN/GaN interfaces.[5]

Experimentally, the band offsets in InGaN/GaN heterostructures have been investigated extensively via a wide variety of techniques, including X-Ray photoemission spectroscopy (XPS), photocurrent spectroscopy, internal photoemission measurements, and capacitance-voltage measurements.[6–12] These studies focus mainly on [0001] InN/GaN heteroepitaxial films consisting of an InN capping layer on thick GaN substrates/templates.[6–11] The *c*-plane cut corresponding to [0001] epitaxy is more commonly

a)Author to whom correspondence should be addressed. Electronic mail: p.alpay@ims.uconn.edu

used than the non-polar and semi-polar orientations because of the ease of availability of single crystal substrates, such as sapphire, onto which these multilayers can be grown. The measured values of InN/GaN valence band offset (ΔE_V) from such structures show a large disparity. ΔE_V is relatively large (0.8−1.1 eV) for capping layers with high defect densities[6] or for relatively thicker capping layers (>200 nm)[8,11] compared with cases where ultrathin capping layers (~5 nm) with a high crystal quality are used (0.5–0.6 eV).[7,10] This is understandable since the electronic structures of InN and GaN change significantly as functions of crystal orientations, in-plane misfit strain, and defect microstructures (misfit and threading dislocations, impurities, phase/grain boundaries, etc.). We also note that for InGaN/GaN MQWs with polar and semi-polar orientations, the strong band bending due to the large built-in electric field, on the order of a few MV/cm,[13] resulting from the polarization difference between adjacent layers must be taken into account.

Density functional theory (DFT) has been employed to investigate the band offsets between InGaN and GaN in the wurtzite structure.[14–16] These studies mainly focus on InN/GaN band offsets,[14,15] although InGaN/GaN MQWs are more commonly used in device applications. The purpose of considering only the binary heterostructures is to reduce the computational cost because InN can be simulated using a relatively small unit cell containing 4 atoms, whereas a disordered InGaN alloy requires a much bigger unit cell (with at least 16 atoms) to properly reproduce its bulk properties.[16–18] Recent results by Moses *et al.*[16] show that ΔE_V of InGaN/GaN at the $(10\bar{1}0)$ *m*-plane interface is a linear function of the In concentration, *x*, in the InGaN alloy from 0 eV (GaN) to 0.62 eV (InN). These calculations are based on the DFT method supplemented by modern hybrid Heyd-Scuseria-Ernzerhof (HSE06) functionals and utilize InGaN unit cells having 16 or 32 atoms for In concentrations of $x = 0.25$, 0.5, and 0.75.[16] Moreover, the selection of the non-polar *m*-plane epitaxy allows carrying out relatively easier computations in which it avoids consideration of the polarization mismatch at the interlayer interfaces. To further simplify the calculations, the analysis is limited to natural band alignments corresponding to strain-free (and unconstrained) InGaN and GaN in the InGaN/GaN MQW constructs. Because GaN-based materials are often deposited on appropriate substrates with a *c*- alignment direction,[19] it is necessary to expand such a theoretical method to InGaN/GaN MQWs with polar interfaces. Obviously, *m*- and *c*-plane orientations have different atomic arrangements (and hence different surface terminations), producing different magnitudes of in-plane misfit strains. As such, these factors need to be incorporated into a theoretical analysis to determine band offsets more accurately, which is the topic of the present paper.

We utilize first-principles calculations to systematically analyze ΔE_V and band bending as a function of composition in heteroepitaxial undoped InGaN/GaN MQWs on *m*-plane and *c*-plane GaN substrates in the presence of in-plane misfit strain. InGaN ternary alloys are treated by relatively large unit cells having 32 atoms for seven In compositions, namely, $x = 0.125$, 0.25,…, 0.875. We show here that ΔE_V for the *m*-plane epitaxy displays a linear increase as *x* varies from 0 to 1 and is relatively insensitive to in-plane misfit strain, while ΔE_V for *c*-plane epitaxy increases non-linearly in the entire composition range and is significantly lower than the corresponding strain-free value for $x \geq 0.5$. For polar InGaN/GaN MQWs, our results indicate that the nonlinear coupling between the in-plane misfit strain and the piezoelectric polarization plays an important role in the extent of band bending within the ultrathin interlayers of such constructs. We also carry out a macroscopic continuum level electrostatic analysis (ESA) based on Maxwell and Poisson's relations to describe the built-in electric field. To determine the polarization in the layers, we employ first- and higher-order piezoelectric coefficients of bulk InGaN and GaN that are determined through DFT. The field strengths obtained from ESA are in good agreement with the results obtained from atomic level DFT calculations with differences usually less than 1 MV/cm, indicating that standard ESA[14] with nonlinear piezoelectric coupling can provide a powerful means of predicting band banding without a detailed DFT analysis.

II. COMPUTATIONAL METHODOLOGY

In our theoretical analysis, GaN and InN are modeled within the framework of their wurtzite crystal structure [Fig. 1(a)]. For the InGaN ternary alloys, we construct a set of orthorhombic/wurtzite equivalent unit cells consisting of 32 atoms (O-32) for seven In compositions, $x = 0.125$, 0.25,…, and 0.875 [see Fig. 1(b), for an example, corresponding to $In_{0.125}Ga_{0.875}N$]. The composition dependence of the atomic structure of the entire set of O-32 unit cells is given in Ref. 20. Such unit cells have been found to be sufficiently large to reproduce the experimentally measured lattice parameters (a_0 and c_0) and band gap bowing in InGaN and ZnO-BeO systems.[18,20] The calculated a_0 (c_0) of bulk InGaN increases per Vegard's law from 3.223 Å (5.239 Å) for $x = 0$ to 3.582 Å (5.786 Å) for $x = 1$.[18] These structures were also utilized to calculate the polarization and elastic and piezoelectric coefficients of bulk InGaN.[18]

In this study, these unit cells are employed to determine ΔE_V between InGaN and GaN under four different mechanical boundary conditions [see Fig. 1(a) for crystal orientations]:

1. *m*-plane strain-free InGaN/GaN bilayers;
2. InGaN/GaN MQWs on *m*-plane GaN substrates with $[1\bar{2}10]_{InGaN}//[1\bar{2}10]_{GaN}$ and $[0001]_{InGaN}//[0001]_{GaN}$ epitaxial alignments;

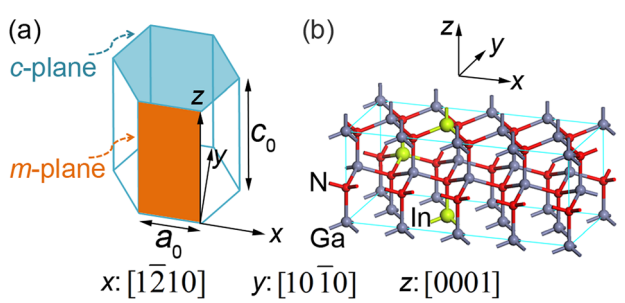

FIG. 1. (a) Schematic wurtzite lattice of GaN (InN) and (b) an example of $In_xGa_{1-x}N$ O-32 unit cell for $x = 0.125$. The *m*- and *c*-planes shown in (a) correspond to *x*-*z* and *x*-*y* planes in (b), respectively.

3. *c*-plane strain-free InGaN/GaN bilayers;
4. InGaN/GaN MQWs on *c*-plane GaN substrates with $[10\bar{1}0]_{InGaN}//[10\bar{1}0]_{GaN}$ and $[1\bar{2}10]_{InGaN}//[1\bar{2}10]_{GaN}$ epitaxial alignments.

To determine ΔE_V between strain-free InGaN and GaN, we employ a stack consisting of an InGaN slab with *m*- (non-polar) or *c*-plane (polar) surfaces exposed to vacuum [Figs. 2(a) and 2(b)]. For a given In composition, the non-polar (polar) InGaN slab contains 14 (16) atomic layers that are constrained to their bulk lattice parameters in the *m*- (*c*-) planes but completely relaxed along the out-of-plane $[10\bar{1}0]$ ([0001]) direction. The vacuum region in such stacks is 20 Å (*m*-plane) or 25 Å (*c*-plane) thick to prevent interactions between periodic images.

To simulate the polar and non-polar epitaxial InGaN/GaN MQWs on GaN substrates, a $(InGaN)_6/(GaN)_6$ superlattice is constructed along the [0001] and $[10\bar{1}0]$ directions as shown in Figs. 2(c) and 2(d), respectively. For the *m*-plane epitaxial condition, GaN is assumed to be strain-free (thick substrate), while in InGaN there exist in-plane compressive strains u_1 and u_3 along the $[1\bar{2}10]$ and [0001] directions, respectively, and a commensurate tensile stress-free strain u_2 along the $[10\bar{1}0]$ direction. The strain conditions in the epitaxial *m*-plane InGaN layers are

$$u_{ij}(m-plane) = \begin{pmatrix} u_1 & 0 & 0 \\ 0 & u_2 & 0 \\ 0 & 0 & u_3 \end{pmatrix}. \quad (1)$$

In Eq. (1), u_1 and u_3 are determined by the differences in lattice parameters a_0 and c_0 [Fig. 1(a)] between bulk (relaxed) InGaN and bulk (relaxed) GaN, respectively. On the other hand, the principal axial strains for InGaN layers for *c*-plane epitaxy are

$$u_{ij}(c-plane) = \begin{pmatrix} u_1 & 0 & 0 \\ 0 & u_1 & 0 \\ 0 & 0 & u_3 \end{pmatrix}, \quad (2)$$

where u_1 is the equi-biaxial in-plane misfit strain, and u_3 is the out-of-plane stress-free strain. The specific values of the strains in Eqs. (1) and (2) are provided in Table I as a function of the In concentration.

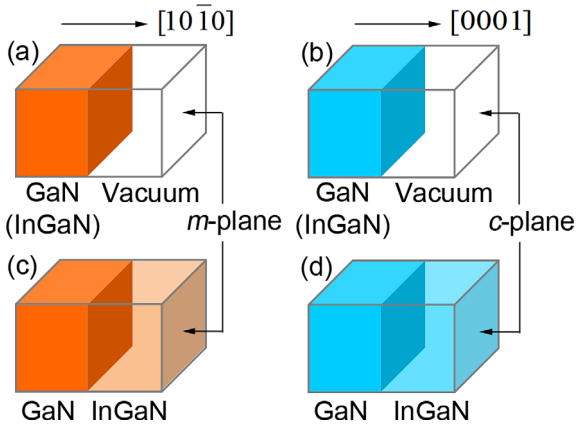

FIG. 2. Heterostructures consisting of GaN (or InGaN) and vacuum region along (a) the nonpolar $[10\bar{1}0]$ direction, (b) the polar [0001] direction. Also shown schematically are (c) *m*- and (d) *c*-plane InGaN/GaN MQWs, respectively.

DFT calculations are carried out using projector augmented wave pseudo-potentials[21] and plane-wave expansions with a cutoff energy of 400 eV as implemented in the VASP code.[22] The Ga 3*d* and In 4*d* electrons are included in their valence states, respectively. The exchange-correlation functional is treated within the PW91 generalized gradient approximations (GGA).[23] We note that while GGA does not predict accurately the absolute band gap energy of semiconductors,[24] the energy difference in the valence band edge of InGaN and GaN (i.e., ΔE_V) is relatively insensitive to the choice of exchange-correlation functional[16] and, therefore, is a powerful approach to band offset calculations. For example, we show in Sec. III that the strain-free ΔE_V at the *m*-plane InGaN/GaN interfaces calculated by GGA is in excellent agreement with previous results[16] produced by the time-intensive hybrid functional HSE06.[25] Thus, the relatively simpler GGA is used for all such calculations in this study. The spontaneous polarization and piezoelectric coefficients of bulk GaN and InGaN are determined by the Berry phase approach as described elsewhere.[18,20] The static dielectric constants are calculated via the density functional perturbation theory as embedded in the VASP code.[26] In bulk computations, a $9\times9\times6$ and $3\times6\times6$ Γ-centered *k*-point mesh in the first Brillouin zone is found to yield well-converged results for GaN (InN) and InGaN. The number of *k*-points is reduced to 1 along the stacking direction of all structures shown in Fig. 2. The atomic positions are optimized until all components of the forces on each atom are reduced to values below 0.02 eV/Å.

III. BAND OFFSETS FOR *m*-PLANE INTERFACES

We begin the analysis of ΔE_V with the non-polar undoped *m*-plane InGaN/GaN interfaces, which are relatively simple to compute due to the absence of polarization-induced charge at the interfaces. We first assume both InGaN and GaN are fully relaxed (strain-free) as in thick layers, corresponding to the mechanical boundary condition (1) in Sec. II. The strain-free ΔE_V is determined by comparing their respective valence band positions (E_V^{GaN} and E_V^{InGaN}) with the energy of vacuum (U^{Vac}) at the *m*-plane surfaces, so that

TABLE I. InGaN as a function of In composition *x* in InGaN/GaN MQWs on *m*- and *c*-plane GaN substrates.

	m-plane			*c*-plane	
x	u_1	u_2	u_3	u_1	u_3
0.125				−0.0119	0.0059
0.25	−0.0252	0.0169	−0.0235	−0.0252	0.0133
0.375				−0.0385	0.0217
0.5	−0.0518	0.0401	−0.0459	−0.0518	0.0309
0.625				−0.0645	0.0416
0.75	−0.0766	0.0663	−0.0704	−0.0766	0.0515
0.875				−0.0884	0.0606
1	−0.1003	0.0920	−0.0946	−0.1003	0.0714

$$\Delta E_V = (U^{Vac} - E_V^{GaN}) - (U^{Vac} - E_V^{InGaN}) \equiv I^{GaN} - I^{InGaN}, \quad (3)$$

where I^{GaN} and I^{InGaN} are the ionization energies of GaN and InGaN, respectively. To derive an expression for I^{GaN}, we employ a three-step process for the *m*-plane GaN stack shown schematically in Fig. 2(a). First, we calculate its electrostatic potential with 3-dimensional periodic boundary conditions. Next, the potential is averaged within each *m*-plane cross-section, which, we find, demonstrates an oscillatory "bulk-like" pattern in the GaN region and a flat band, i.e., U^{Vac} in the vacuum region [see the dashed curve in Fig. 3(a)]. The potential is further averaged over the length of one GaN unit cell along the $[10\bar{1}0]$ direction [shown as the solid line in Fig. 3(a)], leading to a volumetric average of the GaN potential energy (U^{GaN}) at the center of the GaN slab. Finally, I^{GaN} is found by identifying the position of E_V^{GaN} in the same figure. This is easily done since the difference between E_V^{GaN} and U^{GaN} can be determined by a separate calculation that only involves bulk GaN. The above process is similarly applied to InGaN for $x = 0.25$, 0.5, 0.75, and 1. Based on these values, ΔE_V for a strain-free InGaN/GaN heterostructure is calculated using Eq. (3) and is found to vary almost linearly from 0 eV to 0.57 eV as the In composition x increases from 0 to 1 (see Fig. 4). Our results from the relatively simple GGA agree well with those of a previous DFT study using the HSE06 functional.[16]

In the above analysis, both GaN and InGaN are considered to be strain-free and unconstrained. However, the electronic structure of a heterostructure or MQW is very sensitive to misfit strain,[5] which arises from the lattice mismatch between the film and the substrate and/or between adjacent layers. To assess the effect of strain in non-polar InGaN/GaN MQW structures, we investigate pseudomorphic $(InGaN)_6/(GaN)_6$ superlattices on *m*-plane GaN substrates [Fig. 2(c)]. The electrostatic potential of such a superlattice is first averaged over the unit cell length of the strain-free GaN along the $[10\bar{1}0]$ direction and then along the strained InGaN, respectively, to find out the relative positions of U^{GaN} and U^{InGaN} [Fig. 3(b)]. E_V^{GaN} and the valence band position in strained InGaN layers $E_{V'}^{InGaN}$ were determined per Fig. 3(b) without reference to the vacuum energy level. Such a procedure has been applied to other non-polar lattice mismatched heterostructure materials systems, including Si/Ge and GaAs/InAs.[27,28] The calculated ΔE_V in the epitaxial *m*-plane superlattices does not display a large deviation from the corresponding strain-free values for $x = 0.25$, 0.5, and 0.75 (Fig. 4).

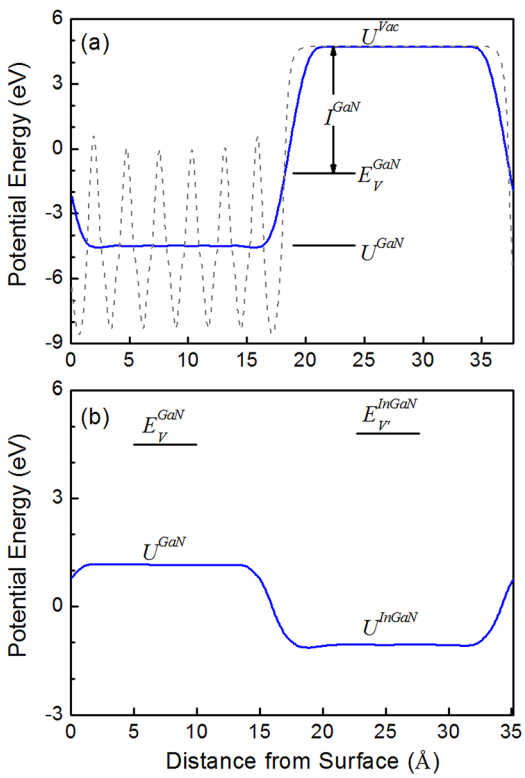

FIG. 3. Electrostatic potentials in (a) an *m*-plane GaN/vacuum heterostructure as shown in Fig. 2(a), and in (b) a $In_{0.5}Ga_{0.5}N$/GaN MQW on an *m*-plane GaN substrate as shown in Fig. 2(c).

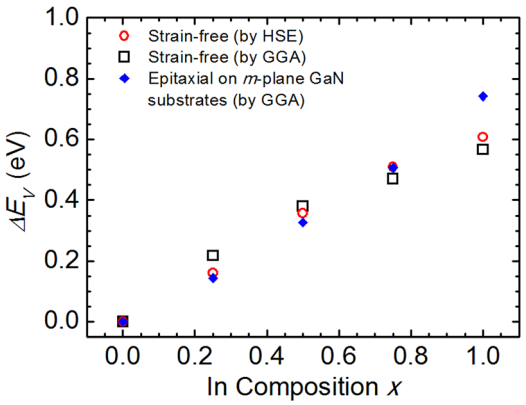

FIG. 4. ΔE_V of *m*-plane InGaN/GaN for two mechanical boundary conditions: strain-free *m*-plane InGaN and GaN slabs (by HSE[16] and GGA), and epitaxial InGaN/GaN MQW on *m*-plane GaN substrate (by GGA).

IV. BAND OFFSETS FOR *c*-PLANE INTERFACES

Polar *c*-plane InGaN/GaN heterostructures and MQWs are important as they lend themselves to practical applications in devices, such as LEDs and lasers, because to large extent the substrates for *c*-plane epitaxy (e.g., sapphire) are relatively inexpensive and the growth techniques are better developed than those in nonpolar or semi-polar orientations.[29] To compute ΔE_V between (0001) InGaN and InN layers, the constructs in Figs. 2(b) and 2(d) are utilized under mechanical boundary conditions (3) and (4) in Sec. II, respectively.

The profiles of the volumetrically averaged electrostatic potential for strain-free InGaN ($0 \le x \le 1$) slabs [Fig. 2(b)] and pseudomorphic $(InGaN)_6/(GaN)_6$ superlattices [Fig. 2(d)] are obtained following the procedure outlined in Sec. III, and are plotted in Figs. 5(a) and 5(b), respectively. For both cases, the inclined potential with respect to the distance from the basal plane (z) indicates the existence of a built-in electric field as a result of the compositional variation along the direction of polarization. The bulk-like potential energies (U^{GaN}, U^{Vac}, and U^{InGaN}) have to be extended to the interfaces (see corresponding arrows in Fig. 5) to calculate ΔE_V under such circumstances. We note that the magnitudes of ΔE_V determined by this procedure are dependent on the selection

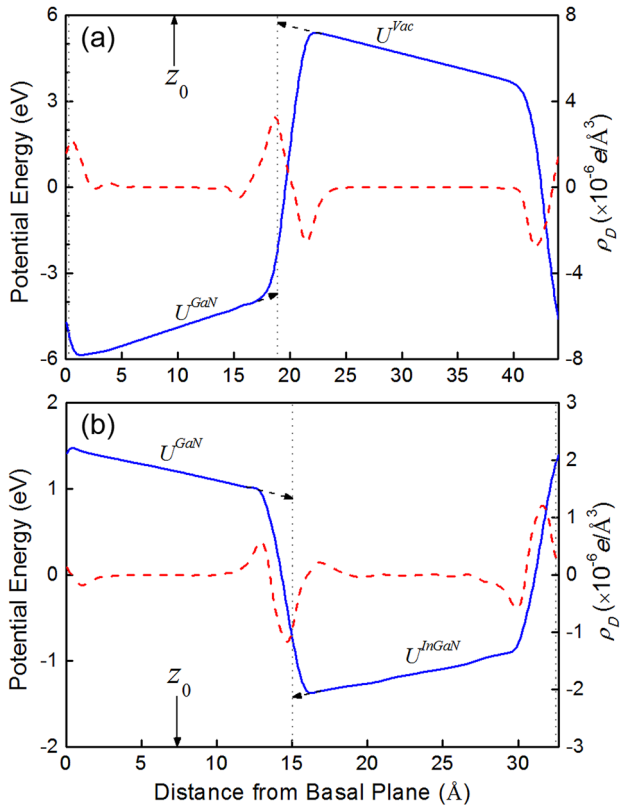

FIG. 5. Electrostatic potentials (solid curve) and bound charge distribution (dashed curve) in (a) a *c*-plane GaN/vacuum slab as shown in Fig. 2(b) and in (b) a $In_{0.5}Ga_{0.5}N$/GaN MQW on a *c*-plane GaN substrate as shown in Fig. 2(d).

of GaN/vacuum or InGaN/GaN interface positions in Fig. 5. In fact, the interfaces span a narrow region (usually within 2 Å in Fig. 5) in which the electrostatic potential changes continuously. Nevertheless, abrupt interface conditions and the corresponding band offsets are favored for designs at larger length scales (μm or higher) in order to simplify the simulations. Thus, to determine the optimal positions of the left and right interface planes, we first identify a folding plane between the two interfaces (z_0 in Fig. 5). For this purpose, we follow the methodology developed by Bernardini and Fiorentini for polar (0001) AlN/GaN superlattices[30] and utilize the bound charge density (ρ_D) that results from the polarization mismatch between GaN and vacuum or between InGaN and GaN. From Fig. 5, one can see that ρ_D is primarily distributed across the interfaces, permitting us to decompose ρ_D into odd and even terms, i.e., a monopole and dipole distribution (ρ_D^{mono} and ρ_D^{dip}) with respect to z_0 such that

$$\rho_D^{mono}(z-z_0) = \frac{1}{2}[\rho_D(z-z_0) - \rho_D(z_0-z)], \quad (4a)$$

$$\rho_D^{dip}(z-z_0) = \frac{1}{2}[\rho_D(z-z_0) + \rho_D(z_0-z)]. \quad (4b)$$

The optimal position for z_0 is chosen so that the dispersions of the monopole and dipole moments ($\int |\rho_D^{mono}(z-z_0)|^2 dz$ and $\int |\rho_D^{dip}(z-z_0)|^2 dz$, respectively) are minimized near the interfaces.[30] Such a criterion results in continuously varying functions and prevents the occurrence of computation singularities. Subsequently, the optimal positions of the interface planes in Fig. 5 are given as $z_0 \pm 0.5L^{GaN}$, where L^{GaN} is the thickness of GaN region.

It is interesting to note that in Fig. 5(a), the calculated potential offsets at the left and right interfaces are unequal, due to the asymmetric surface terminations of the GaN slab, i.e., the left and right *c*-plane surfaces are terminated with a pure Ga and N atomic layer, respectively. Similar phenomena occur in InGaN/GaN superlattices [Fig. 5(b)] because the left and right interfaces are composed of N-Ga bonds and N-(In, Ga) bonds, respectively. The average of the two potential offsets is used throughout the calculations to determine ΔE_V. In both strain-free InGaN/GaN bilayers and epitaxial MQWs on GaN substrates, ΔE_V increases nonlinearly (Fig. 6) as x varies from 0 (GaN) to 1 (InN). ΔE_V in pseudomorphic (0001) InGaN/GaN superlattices is reduced compared with the corresponding strain-free value. The decrease in ΔE_V for InGaN/GaN superlattices can be attributed to the dependence of the band structure of InGaN on the lattice deformation. The compressive equi-biaxial misfit strain u_1 and the commensurate out-of-plane strain u_3 shift the valence band edge of InGaN down from its strain-free energy level. As the In concentration increases, u_1 in InGaN grows as well from 0 ($x=0$, GaN) to -10% ($x=1$, InN) per Vegard's law (Table I). Therefore, the decrease in ΔE_V becomes more significant for higher In compositions ($x \geq 0.5$).

The calculated strain-free ΔE_V of InN/GaN for *c*-plane epitaxy (0.90 eV) agrees well with experimental results (0.94−0.95 eV) reported by Wang *et al.* using a 200 nm-thick InN capping layer with a dislocation density of approximately 4×10^{-11} cm^{-2} on a (0001) GaN template.[8] Our calculations indicate that ΔE_V in pseudomorphic (0001) InN/GaN superlattice is 0.64 eV, in good agreement with 0.58 ± 0.08 eV measured by King *et al.* for 5 nm thick (0001) InN on GaN samples.[10]

V. MACROSCOPIC ELECTROSTATIC ANALYSIS

From the DFT calculated electrostatic potential shown in Fig. 5(b), one can observe that the internal electric field induced by the bound sheet charge results in band bending at the polar InGaN/GaN interfaces. This band bending in polar MQWs produces a spatial separation of the electron and the

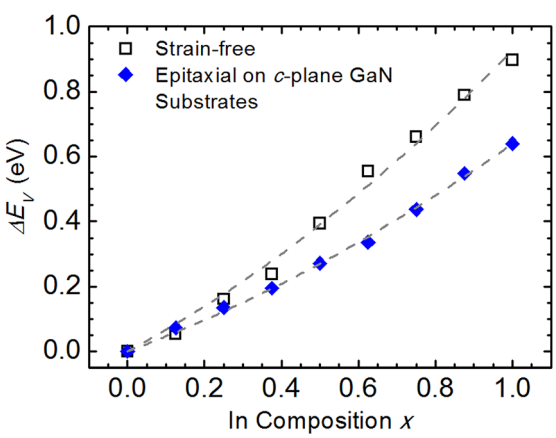

FIG. 6. ΔE_V for strain-free *c*-plane InGaN/GaN slabs and epitaxial InGaN/GaN MQWs on *c*-plane GaN substrate.

hole wave-functions and an accumulation of 2-dimensional electron and/or hole gases at the interlayer interfaces. Hence, the built-in electric field is an important parameter that affects the electronic and optoelectronic properties of polar InGaN/GaN MQWs.

The built-in electric field in the polar InGaN/GaN MQWs can be obtained from the slope of the DFT-calculated electrostatic potential shown in Fig. 5(b). This approach is non-parametric, meaning that it does not refer to the existing knowledge of properties of InGaN or GaN. It is based on the quantum mechanical description of the atomistic interactions in such InGaN/GaN MQWs, and provides the most reliable description of the electrostatic conditions in such ultra-thin multilayer structures. However, such DFT calculations are extremely time-intensive compared with continuum level modeling. We develop here an ESA for epitaxial (0001) InGaN/GaN MQWs on GaN substrates to confirm the internal electric fields and bound charge density obtained via DFT [Fig. 5(b)]. Such an ESA keeps the precision as high as DFT calculations while it significantly reduces the computational cost for future device designs because it only takes the *bulk* materials properties of InGaN and GaN as input parameters. Unfortunately, some key parameters, such as the spontaneous polarization and piezoelectric coefficients of InGaN, have not been measured experimentally. These are provided through our DFT calculations of *bulk* InGaN and GaN.

To start off the ESA, we assume that GaN barrier layers are strain-free and the total polarization in GaN is equal to its spontaneous polarization ($P_S^{\mathrm{GaN}} = -0.0329\,\mathrm{C/m^2}$). In the InGaN layer, in addition to the spontaneous polarization P_S^{InGaN}, equi-biaxial in-plane strain u_1 and the out-of-plane strain u_3 result in a strong piezoelectric polarization P_{PZ}^{InGaN} (Table II). While most device simulations assume a linear (first-order) coupling between the polarization and strain, recent theoretical and experimental findings indicate that second-order piezoelectric coupling may be significant in the III-nitrides semiconductor family of AlN, GaN, and InN and their alloys.[31,32] In our methodology, the polarization for *bulk* InGaN under the strain condition given by Eq. (2) is obtained through DFT calculations based on the Berry-phase approach. Our results show that P_{PZ}^{InGaN} can be described via

$$P_{PZ}^{\mathrm{InGaN}} = Au_1 + Bu_1^2 + Cu_3 + Du_3^2, \tag{5}$$

where A and C are the first-order and B and D are the second-order piezoelectric coefficients, respectively. These are obtained from our DFT computations for all seven In compositions considered in this study and are provided in Table II along with P_S^{InGaN} and P_{PZ}^{InGaN} in polar InGaN/GaN MQWs.

TABLE II. Piezoelectric coefficients A, B, C, and D of bulk InGaN, and P_S, and P_{PZ} of InGaN in InGaN/GaN MQWs on c-plane GaN substrates (units: $\mathrm{C/m^2}$).

x	A	B	C	D	P_S^{InGaN}	P_{PZ}^{InGaN}
0.125	−0.6686	11.6062	0.6336	−12.7135	−0.0357	0.0127
0.25	−0.8973	12.4622	0.8744	−10.3529	−0.0296	0.0404
0.375	−0.7723	13.6241	0.8312	−12.8380	−0.0479	0.0620
0.5	−0.7925	11.0730	0.8958	−12.0420	−0.0521	0.0863
0.625	−0.8235	12.4913	0.9130	−10.6886	−0.0514	0.1246
0.75	−1.1307	9.6243	0.8589	−15.9317	−0.0500	0.1451
0.875	−1.2627	−0.5682	1.1558	−8.1965	−0.0468	0.1471

Built-in electric fields arise from the polarization mismatch between the barrier and well layers in the polar MQWs. At finite temperatures, the electric fields produce two-dimensional electron and/or hole accumulation at the interlayer interfaces. DFT calculations are performed at 0 K and to be able to compare these results to ESA, the inherent assumption in the calculations that follow is that all carriers are frozen and there are no free charges at the interfaces. Under these conditions, the relevant Maxwell's equation describing dielectric displacement is[30]

$$\begin{aligned} D &= \varepsilon_0 \kappa^{\mathrm{GaN}} E^{\mathrm{GaN}} + P_S^{\mathrm{GaN}} \\ &= \varepsilon_0 \kappa^{\mathrm{InGaN}} E^{\mathrm{InGaN}} + P_S^{\mathrm{InGaN}} + P_{PZ}^{\mathrm{InGaN}}, \end{aligned} \tag{6}$$

where D is the total electric displacement, ε_0 is the permittivity of vacuum, κ^{GaN} (κ^{InGaN}) is the static dielectric constant of GaN (InGaN), and E^{GaN} (E^{InGaN}) is the built-in electric field in the GaN (InGaN) layer. κ^{GaN} and κ^{InN} obtained by our DFT calculations (11.71 and 15.28, respectively) are in agreement with experimental results (10. 4 and 14.4, respectively).[33,34] Our computations also show that κ^{InGaN} varies almost linearly from 11.71 to 15.28 as x increases from 0 (GaN) to 1 (InN).

The DFT potential profile of the (0001) InGaN/GaN superlattice shown in Fig. 5(b) is obtained using standard 3-dimensional periodic boundary conditions. In the continuum limit, the total electrical potential in an open circuit condition along the [0001] direction is

$$E^{\mathrm{GaN}} L^{\mathrm{GaN}} + \Delta U_1 + E^{\mathrm{InGaN}} L^{\mathrm{InGaN}} - \Delta U_2 = 0, \tag{7}$$

where L^{GaN} and L^{InGaN} are the thicknesses of GaN and InGaN layers, respectively, and are given by $L^{\mathrm{GaN}} = 3c_0^{\mathrm{GaN}}$ and $L^{\mathrm{InGaN}} = 3(1+u_3)c_0^{\mathrm{InGaN}}$. Here, c_0^{GaN} and c_0^{InGaN} are the lattice parameters of bulk GaN and InN along the [0001] direction, respectively. Also entering Eq. (7) are ΔU_1 and ΔU_2 which correspond to the potential offsets at the left and the right interfaces, respectively. Combining Eqs. (6) and (7), E^{GaN} is obtained as follows:

$$E^{\mathrm{GaN}} = \frac{L^{\mathrm{InGaN}}\left(P_S^{\mathrm{InGaN}} + P_{PZ}^{\mathrm{InGaN}} - P_S^{\mathrm{GaN}}\right) - \kappa^{\mathrm{InGaN}}\left(\Delta U_1 - \Delta U_2\right)}{\varepsilon_0\left(\kappa^{\mathrm{GaN}} L^{\mathrm{InGaN}} + \kappa^{\mathrm{InGaN}} L^{\mathrm{GaN}}\right)}. \tag{8}$$

In Eq. (8), the second term of the numerator is much smaller compared with the first term for all seven In compositions chosen. Therefore, Eq. (8) can be simplified as follows:

$$E^{\mathrm{GaN}} \approx \frac{L^{\mathrm{InGaN}}\left(P_S^{\mathrm{InGaN}} + P_{PZ}^{\mathrm{InGaN}} - P_S^{\mathrm{GaN}}\right)}{\varepsilon_0\left(\kappa^{\mathrm{GaN}} L^{\mathrm{InGaN}} + \kappa^{\mathrm{InGaN}} L^{\mathrm{GaN}}\right)}. \tag{9}$$

Similarly,

$$E^{\mathrm{InGaN}} \approx -\frac{L^{\mathrm{GaN}}\left(P_S^{\mathrm{InGaN}} + P_{PZ}^{\mathrm{InGaN}} - P_S^{\mathrm{GaN}}\right)}{\varepsilon_0\left(\kappa^{\mathrm{GaN}} L^{\mathrm{InGaN}} + \kappa^{\mathrm{InGaN}} L^{\mathrm{GaN}}\right)}. \tag{10}$$

Based on the built-in electric fields, the total polarization in GaN and InGaN layer is given by

$$P_T^{GaN} = \varepsilon_0(\kappa^{GaN} - 1)E^{GaN} + P_S^{GaN}, \quad (11a)$$

$$P_T^{InGaN} = \varepsilon_0(\kappa^{InGaN} - 1)E^{InGaN} + P_S^{InGaN} + P_{PZ}^{InGaN}. \quad (11b)$$

Combining Eqs. (6) and (11), the polarization mismatch at the interlayer interfaces, i.e., the bound sheet charge density (σ_D) is

$$\sigma_D = P_T^{InGaN} - P_T^{GaN} = \varepsilon_0(E^{GaN} - E^{InGaN}). \quad (12)$$

The ESA calculated built-in electric fields and the bound sheet charge densities are given in Table III. There is an excellent agreement between ESA and atomic-level DFT computations. The accuracy of ESA in this study is significantly improved by taking into account second-order piezoelectric coupling established via DFT when compared with a previous theoretical study for (0001) InN/GaN MQWs that only considers first-order piezoelectric coefficients.[14]

We note that at temperatures above 0 K, internal electric fields due to the bound sheet charges may partially be screened by the formation of 2-dimensional electron/hole gases at the interfaces. The density of such free carries or the density of the 2-dimensional electron gases in epitaxial *c*-plane InGaN/GaN MQWs has been determined using empirical relations taking into account the bound charge density, relative position of Fermi Energy, and the conduction band offset.[13]

VI. DISCUSSION AND CONCLUSIONS

The results regarding the role of mechanical boundary conditions and the compositional variations on the band bending and band offsets in InGaN/GaN MQWs have several implications related to how optoelectronic properties of such constructs can be optimized by tuning ΔE_V. The valence band offset increases with In concentration in InGaN/GaN superlattices regardless of the mechanical boundary conditions and those associated with epitaxial growth. While this is a well-known result, this general conclusion provides a sanity check for the theoretical approach, providing confidence that the analysis is able to meet the basic experimental observations. For In compositions $x < 0.5$, our calculations show that nonpolar and polar MQWs yield similar ΔE_V values. The valence band offset is enhanced in the case of a polar *c*-plane orientation for In concentrations larger than 0.5, where field effects due to the polarization must be accounted for. For non-polar *m*-plane InGaN/GaN MQWs, the role of epitaxial strains, which increases with increasing In concentration according to Vegard's law, has a very little effect on ΔE_V for $x < 0.8$. On the other hand, the difference between the valence band offset of strained and stress-free *c*-plane MQWs is substantial, especially for relatively large In concentrations ($x > 0.5$).

TABLE III. The magnitudes of built-in electric fields E^{GaN} and E^{InGaN} (unit: MV/cm) and bound sheet charge densities σ_D (unit: $\mu C/cm^2$) obtained by DFT and ESA.

	DFT			ESA		
x	E^{GaN}	E^{InGaN}	σ_D	E^{GaN}	E^{InGaN}	σ_D
0.125	0.54	−0.51	0.100	0.48	−0.47	0.093
0.25	1.35	−1.39	0.320	1.79	−1.72	0.335
0.375	2.19	−2.20	0.386	2.21	−2.09	0.389
0.5	3.71	−3.60	0.584	3.14	−2.90	0.647
0.625	5.04	−4.55	0.882	4.93	−4.46	0.849
0.75	6.73	−5.30	0.756	5.92	−5.23	1.065
0.875	8.77	−6.81	1.322	6.14	−5.30	1.379

An important conclusion of the above findings is that a combination of mechanical boundary conditions (constrained vs. unconstrained), choice of orientation, and the In concentration are important levers in the design parameters of unique optoelectronic devices. To that end, we note that the in-plane misfit strain in pseudomorphic heteroepitaxial InGaN/GaN superlattices considered in this study from both atomistic and continuum level simulations can reach as high as 10% (InN/GaN). For *c*-plane epitaxial conditions, our results suggest that for InGaN/GaN with high In concentration, the in-plane misfit strain reduces ΔE_V and thus increases the conduction band offset, resulting in an enhancement in quantum confinement for conduction electrons and hence the electronic properties of MQWs, where coupling to the confined 2-dimensional gas can possibly lead to new devices with substantially improved properties. However, such an extremely high internal strain would (if not controlled through careful materials tailoring) certainly be relaxed via the formation of defects (misfit dislocations, delamination, and cracking) for film thicknesses larger than a few unit cells. A straightforward application of the Matthews–Blakeslee (MB) criterion[35] shows that for $0.05 \le x \le 0.3$, the critical thickness for misfit dislocation formation varies from 20 nm to 2 nm and from 100 nm to 15 nm for an epitaxial InGaN layer on *c*- and *m*-plane GaN substrates, respectively.[36,37] For higher In concentrations, the MB critical film thickness is even smaller, of the order of one unit cell. The formation of interfacial dislocations may partially or fully relax the in-plane misfit strain, reducing the magnitude of built-in electric fields within the multilayer structure. Their actual values may vary depending on the strain state and the defect microstructure of the specific MQWs.

The internal electric fields caused by the polarization mismatch and the strain due to the lattice mismatch are volumetric quantities. While the introduction of dislocation network results in global relaxation of the mechanical strains, it also produces localized strain fields of the order of the characteristic length of dislocations (magnitude of the Burgers vector). In a piezoelectric medium, spatial variations in stress/strain conditions immediately generate localized electrostatic fields around the defects.[38,39] A previous theoretical study by Shi *et al.* has shown that defect induced charge densities at the surfaces of GaN may reach up to 10^{11} e/cm^2 within a distance of 100 nm from the dislocation core.[40] As a result, optoelectronic properties of InGaN/GaN-based devices would actually be degraded because of the inelastic scattering of free carriers from the charged defects.

Recent advances in thin film growth technologies [molecular beam epitaxy (MBE) and metal-organic chemical vapor deposition (MOCVD)] now allow the deposition of thin films one atomic layer at a time. Such techniques have been used to synthesize pseudomorphic (0001) InGaN/GaN MQWs at the nanometer scale (i.e., superlattices) with low In concentrations ($x \leq 0.15$).[41,42] For such superlattices, our results show that DFT and ESA can be used to determine the band offset ΔE_V, the internal electric fields, and the bound sheet charge density σ_D quite accurately. It is also important to note that high-quality (0001) InGaN/GaN superlattices that are vertically aligned in one-dimensional nano-rod constructs can be synthesized via MOCVD and hydride vapor phase epitaxy with In concentrations $x > 0.15$.[43,44] However, this configuration corresponds to a different set of mechanical boundary conditions compared with the thin film structures considered in this report. Smaller internal strains and lower defect densities can be achieved in such nanostructures because of the elimination of the 2-dimensional mechanical constraint imposed by the substrate and an increase in surface area made possible by the nano-rod geometry which acts as a sink for point and line defects.

In conclusion, we have carried out *ab initio* calculations based on DFT and a basic electrostatic analysis to study the valence band offsets and band bending for non-polar *m*-plane and polar *c*-plane InGaN/GaN heteroepitaxial MQWs. The atomistic DFT computations and the macroscopic ESA are in excellent agreement, providing experimentalists predictive and self-consistent tools for such a multilayer construct with ultrathin InGaN and GaN layers. Our results show that the valence band offset may be engineered through a combination of variables, including mechanical boundary conditions, epitaxy, and In concentration. Since the electronic band structure of InGaN/GaN heterostructures and quantum wells can be completely characterized by band offsets and internal electric fields, the results of this research can be directly applied in the design of current and potential electronic and optoelectronic devices based on these material systems to achieve optimal device performance.

ACKNOWLEDGMENTS

The research at VCU has been funded by grants from the Air Force Office of Scientific Research and National Science Foundation.

[1]S. Nakamura, Science **281**, 956 (1998).
[2]J. Wu, J. Appl. Phys. **106**, 011101 (2009).
[3]B. N. Pantha, J. Li, J. Y. Lin, and H. X. Jiang, Appl. Phys. Lett. **93**, 182107 (2008).
[4]T. Kuykendall, P. Ulrich, S. Aloni, and P. Yang, Nature Mater. **6**, 951 (2007).
[5]M. Peressi, N. Binggeli, and A. Baldereschi, J. Phys. D: Appl. Phys. **31**, 1273 (1998).
[6]G. Martin, A. Botchkarev, A. Rockett, and H. Morkoç, Appl. Phys. Lett. **68**, 2541 (1996).
[7]C. F. Shih, N. C. Chen, P. H. Chang, and K. S. Liu, Jpn. J. Appl. Phys. Part 1 **44**, 7892 (2005).
[8]K. Wang, C. X. Lian, N. Su, and D. Jena, Appl. Phys. Lett. **91**, 232117 (2007).
[9]Z. H. Mahmood, A. P. Shah, A. Kadir, M. R. Gokhale, S. Ghosh, A. Bhattacharya, and B. M. Arora, Appl. Phys. Lett. **91**, 152108 (2007).
[10]P. D. C. King, T. D. Veal, C. E. Kendrick, L. R. Bailey, S. M. Durbin, and C. F. McConville, Phys. Rev. B **78**, 033308 (2008).
[11]C. L. Wu, H. M. Lee, C. T. Kuo, C. H. Chen, and S. Gwo, Appl. Phys. Lett. **92**, 162106 (2008).
[12]C. T. Kuo, K. K. Chang, H. W. Shiu, C. R. Liu, L. Y. Chang, C. H. Chen, and S. Gwo, Appl. Phys. Lett. **99**, 122101 (2011).
[13]O. Ambacher, J. Majewski, C. Miskys, A. Link, M. Hermann, M. Eickhoff, M. Stutzmann, F. Bernardini, V. Fiorentini, V. Tilak, B. Schaff, and L. F. Eastman, J. Phys.: Condens. Matter **14**, 3399 (2002).
[14]Z. Romanowski, P. Kempisty, K. Sakowski, P. Strak, and S. Krukowski, J. Phys. Chem. C **114**, 14410 (2010).
[15]C. C. Shieh, X. Y. Cui, B. Delley, and C. Stampfl, J. Appl. Phys. **109**, 083721 (2011).
[16]P. G. Moses, M. S. Miao, Q. M. Yan, and C. G. Van de Walle, J. Chem. Phys. **134**, 084703 (2011).
[17]H. J. Xiang, S. H. Wei, J. L. F. Da Silva, and J. B. Li, Phys. Rev. B **78**, 193301 (2008).
[18]L. Dong and S. P. Alpay, J. Mater. Sci. **47**, 7587 (2012).
[19]L. Liu and J. H. Edgar, Mater. Sci. Eng. R. **37**, 61 (2002).
[20]L. Dong and S. P. Alpay, Phys. Rev. B **84**, 035315 (2011).
[21]P. E. Blochl, Phys. Rev. B **50**, 17953 (1994).
[22]G. Kresse and J. Furthmüller, Phys. Rev. B **54**, 11169 (1996).
[23]J. P. Perdew, J. A. Chevary, S. H. Vosko, K. A. Jackson, M. R. Pederson, D. J. Singh, and C. Fiolhais, Phys. Rev. B **46**, 6671 (1992).
[24]L. J. Sham and M. Schlüter, Phys. Rev. Lett. **51**, 1888 (1983).
[25]J. Heyd, G. E. Scuseria, and M. Ernzerhof, J. Chem. Phys. **118**, 8207 (2003).
[26]M. Gajdos, K. Hummer, G. Kresse, J. Furthmuller, and F. Bechstedt, Phys. Rev. B **73**, 045112 (2006).
[27]L. Colombo, R. Resta, and S. Baroni, Phys. Rev. B **44**, 5572 (1991).
[28]N. Tit, M. Peressi, and S. Baroni, Phys. Rev. B **48**, 17607 (1993).
[29]H. Masui, S. Nakamura, S. P. DenBaars, and U. K. Mishra, IEEE Trans. Electron Devices **57**, 88 (2010).
[30]F. Bernardini and V. Fiorentini, Phys. Rev. B **57**, R9427 (1998).
[31]F. Bernardini and V. Fiorentini, Phys. Rev. B **64**, 085207 (2001).
[32]V. Fiorentini, F. Bernardini, and O. Ambacher, Appl. Phys. Lett. **80**, 1204 (2002).
[33]A. S. Barker, Jr. and M. Ilegems, Phys. Rev. B **7**, 743 (1973).
[34]V. Y. Davydov, V. V. Emtsev, I. N. Goncharuk, A. N. Smirnov, V. D. Petrikov, V. V. Mamutin, V. A. Vekshin, S. V. Ivanov, M. B. Smirnov, and T. Inushima, Appl. Phys. Lett. **75**, 3297 (1999).
[35]J. W. Matthews and A. E. Blakeslee, J. Cryst. Growth **27**, 118 (1974).
[36]D. Holec, P. Costa, M. J. Kappers, and C. J. Humphreys, J. Cryst. Growth **303**, 314 (2007).
[37]P. S. Hsu, M. T. Hardy, E. C. Young, A. E. Romanov, S. P. DenBaars, S. Nakamura, and J. S. Speck, Appl. Phys. Lett. **100**, 171917 (2012).
[38]A. N. Stroh, Philos. Mag. **3**, 625 (1958).
[39]S. P. Alpay, I. B. Misirlioglu, V. Nagarajan, and R. Ramesh, Appl. Phys. Lett. **85**, 2044 (2004).
[40]C. Shi, P. M. Asbeck, and E. T. Yu, Appl. Phys. Lett. **74**, 573 (1999).
[41]C. Boney, D. Starikov, I. Hernandez, R. Pillai, and A. Bensaoula, J. Vac. Sci. Technol. B **29**, 03C106 (2011).
[42]Y. K. Noh, M. D. Kim, and J. E. Oh, J. Appl. Phys. **110**, 123108 (2011).
[43]H.-M. Kim, Y.-H. Cho, H. Lee, S. I. Kim, S. R. Ryu, D. Y. Kim, T. W. Kang, and K. S. Chung, Nano Lett. **4**, 1059 (2004).
[44]Q. M. Li, K. R. Westlake, M. H. Crawford, S. R. Lee, D. D. Koleske, J. J. Figiel, K. C. Cross, S. Fathololoumi, Z. T. Mi, and G. T. Wang, Opt. Express **19**, 25528 (2011).